Original Paper

Surface lurking and interfacial ion release strategy for fabricating a superhydrophobic coating with scaling inhibition

Ming-Liang Zhu [a], Hui-Juan Qian [a, b], Wei-Hao Fan [a], Chi-Jia Wang [a], Rui-Xia Yuan [a], Qing-He Gao [b], Huai-Yuan Wang [a, *]

[a] College of Chemistry and Chemical Engineering, Northeast Petroleum University, Daqing, 163318, China
[b] College of Chemical Engineering, Daqing Normal University, Daqing, 163712, China

ARTICLE INFO

ABSTRACT

The design and manufacture of anti-scaling surface is a prospective way to prevent scaling in oil field. In this work, a novel superhydrophobic Cu^{2+}-loaded and DTPMPA-modified anodized copper oxide (S$-Cu^{2+}$/D-ACO) coating was fabricated by modification of 1H,1H,2H,2H-perfluorodecyltriethoxysilane. The valid storing of scale inhibitors at the coating surface and the interfacial release of Cu^{2+} ions contribute to enhancing the anti-scaling of the S$-Cu^{2+}$/D-ACO coating. The water contact angle of the S$-Cu^{2+}$/D-ACO coating is 163.03° and exhibits superhydrophobicity, which makes it difficult for $CaCO_3$ to deposit at the surface of the coating. DTPMPA will steadily lurk into the inner space, and Cu^{2+} will be loaded at the interface in the form of the DTPMPA:Cu^{2+} chelate. During the deposition of $CaCO_3$, the dynamic release of DTPMPA can be realized by transferring DTPMPA:Cu^{2+} to DTPMPA:Ca^{2+}. Interestingly, the released Cu^{2+} hinders the active growth of $CaCO_3$. After 48 h of scaling, the mass of $CaCO_3$ scale at the S$-Cu^{2+}$/D-ACO coating surface is only 44.1% that of the anodized copper oxide coating. The excellent anti-scaling performance of the S$-Cu^{2+}$/D-ACO coating is determined by the synergistic effect of the DTPMPA lurking and dynamic release, as well as the Cu^{2+} inhibition at the interface of superhydrophobic coating and against $CaCO_3$ deposition. This research provides a new exploration for designing and fabricating anti-scaling superhydrophobic surface for oil field development.

1. Introduction

Scale formation is unavoidable in the petroleum industry, electronics, heat exchangers, power generators, water treatment machine and the related industries (Sharma and Gupta, 2020; Zhu et al., 2021a; Jin et al., 2021), especially in the process of alkaline surfactant polymer (ASP) flooding. Due to the use of strong alkali (sodium hydroxide) in ASP flooding, complex physical and chemical reactions will occur between alkali, reservoir rock and formation water in the process of displacement, resulting in the decline of reservoir permeability and scale deposition. Calcium carbonate ($CaCO_3$) is the most common scale in petroleum industry (Edvardsen et al., 2020; Plummer and Busenberg, 1982). The precipitation of $CaCO_3$ in oil field pipelines will adhere to the surface following temperature change and result in scale formation. $CaCO_3$

scale will lead to injection pressure increase, flow rate reduction, pipeline clogging, energy consumption, oil well productivity decrease and other consequences (Wang et al., 2019; Ghosh et al., 2019). To alleviate the serious problems caused by deposition of inorganic salts (e.g. $CaCO_3$, $CaSO_4$, $MgCO_3$), researchers have widely studied some chemicals and scale inhibitors, including diethylene triamine pentamethylene phosphonic acid (DTPMPA), ethylenediamine tetraacetic acid (EDTA), ethylenediaminetetramethylene phosphonic acid (EDTMP), and 1-hydroxyethylidene-1,1-diphosphonic acid (HEDP) (Khormali and Petrakov, 2016; Kan et al., 2020; Mpelwa and Tang, 2019). On the one hand, scale inhibitors can form complexes with cations (e.g. Ca^{2+}, Mg^{2+}) to inhibit the combination of cations with anions (e.g. CO_3^{2-}, SO_4^{2-}). On the other hand, the complexes' asymmetric morphology will inhibit the scale formation by weakening the adhesion between the complexes and pipeline surface. Though the use of scale inhibitor can moderately inhibit scaling, their applications, especially in flowing medium systems, is still limited by high cost, low efficiency

and relevant environmental problems.

The design and preparation of anti-scaling surface is a novel way to prevent scaling from the perspective of the fluid and surface interface (Zhu et al., 2021b). Superhydrophobic coatings with water contact angle (WCA) larger than 150° have attracted much attention owing to the important application in basic research and industries, such as self-cleaning, fluidic drag reduction, anti-fouling, oil-water separation, and anti-corrosion (Dong et al., 2020; Li et al., 2019). However, the research on scale inhibition of superhydrophobic coating is still limited. We previously fabricated a superhydrophobically aluminium-based coating with anti-scaling performance (Zhu et al., 2021b). Nevertheless, a new strategy and efficient storing of the scale inhibitor in the superhydrophobic coating is still urgent to be study.

Copper (Cu) is widely used in industries, including petroleum, machinery manufacturing, light, construction and national defense owing to its excellent electrical and thermal conductivity, and the ease of casting, welding and cutting (Feng et al., 2018). Brass, a Cu and zinc (Zn) alloy with high strength and corrosion resistance, is potentially applicable in petroleum industry, heat exchanger, machine parts and the ship-building industry. However, the surface scaling of Cu and its alloy is also inevitable in some alkaline media especially in tertiary oil recovery. Therefore, improving the performance of copper and copper alloy has become a hot-spot research in recent years. Various studies indicate the control of surface wettability may be a perfect strategy. A superhydrophobic surface with a coral-like micro structure can be obtained by electrochemical oxidation of the copper substrate (Guo et al., 2015). Moreover, the easy-to-clean superhydrophobic Cu/CuO films fabricated by magnetron sputtering show the outstanding corrosion resistance (An et al., 2020). The superhydrophobic zinc oxide coating on the Cu substrate was prepared, and the corresponding anti-icing performance was tested (Yin et al., 2020). A superhydrophobic copper mesh with $Cu(OH)_2$ nano needle arrays has demonstrated the oil-water separation capability (Ren et al., 2018). In addition, the fluorine-free ZnO/CuO superhydrophobic surface has high underwater stability and excellent wear resistance (Velayi and Norouzbeigi, 2019). It can be predicted that it is feasible to prepare copper based superhydrophobic anti-scaling coatings.

Polydopamine (PDA) is an important and appealing bio-mimetic material from mussel (Liu et al., 2019). Self-aggregation or autoxidation of dopamine (DA) is spontaneous at any surface in an alkaline environment, which forms the PDA coating. The existence of plenty active groups such as amino (-NH₂) and hydroxyl (-OH) (Wang et al., 2018) endows PDA with strong adhesion and immobilization ability at either organic or inorganic surface (Wang et al., 2017), and become a modification platform as an intermediate layer to facilitate subsequent surface functionalization (Zhang et al., 2016). Based on the PDA interface adjustment, the superhydrophobic Janus film shows excellent separation ability of oil-water emulsion (Xie et al., 2021). In addition, the film formed by the co-deposition of poly (sulfobetaine methacrylate) and PDA demonstrates good anti-fouling function (Zhou et al., 2014; Zhang et al., 2017). Hence, PDA is potentially applicable for fabrication of superhydrophobic anti-scaling coatings, especially chelating with cations, such as Cu^{2+} and Ca^{2+} (Dou et al., 2019). As far as we know, there is rare report on preparation of copper-based anti-scaling superhydrophobic coating with PDA as the intermediate action layer.

In this work, a novel DTPMPA-modified and Cu^{2+}-loaded superhydrophobic anodized copper oxide (S−Cu^{2+}/D-ACO) coating was fabricated. The special anti-scaling mode of the S−Cu^{2+}/D-ACO coating originates from the scale inhibitor (DTPMPA) pre-storage and the Cu^{2+} stabilized chelate (DTPMPA:Cu^{2+}). Specifically, the Cu^{2+} ions play important role in preventing $CaCO_3$ scaling formation at the S−Cu^{2+}/D-ACO coating surface. The released Cu^{2+} is more inclined to complex with CO_3^{2-} than Ca^{2+}, which will prevent the combination of Ca^{2+} and CO_3^{2-}, and obviously enhance the anti-scaling of the S−Cu^{2+}/D-ACO coating. The morphology, functional groups, crystal structure, and element distribution of the S−Cu^{2+}/D-ACO coating were analyzed by scanning electron microscope (SEM), fourier transformation infrared spectroscopy (FTIR), X-ray diffraction (XRD), and X-ray photoelectron spectrometer (XPS), respectively. The corresponding scale preventing mechanism of the S−Cu^{2+}/D-ACO coating was deeply discussed. This study provides a promising way for the effective storage of scale inhibitors and the preparation of stable superhydrophobic anti-scaling coatings in petroleum industry.

2. Experimental

2.1. Materials and reagents

Pure copper sheets (T2, 99.9 wt% Cu, 20 × 50 × 1 mm³) and copper alloy sheets (H62, 62 wt% Cu and 38 wt% Zn, 10 × 50 × 1 mm³) were supplied by Shanghai Huahong Intelligent Technology Co., Ltd (China). DTPMPA ($C_9H_{28}O_{15}N_3P_5$, Shandong Xintai Water Treatment Technology Co., Ltd., China), 1H,1H,2H,2H-perfluorodecyl triethoxysilane (PFDS, Shanghai McLin Biochemical Technology Co., Ltd), and tris-(hydroxymethyl)-aminomethane (Tris, 99.9 wt%, Suzhou Tianke Intelligent Technology Co., Ltd) were used here. Other materials included dopamine hydrochloride (99.8%, Hefei Bomei Biotechnology Co., Ltd), HCl (guaranteed reagent, 36−38 wt%, Harbin Science and Technology Chemical Reagent Co., Ltd), and H₂O₂ (Tianjin Kermel Chemical Reagent Co., Ltd). Copper sulphate (CuSO₄, Tianjin FengChuan Chemical Reagent Technology Co., Ltd), calcium nitrate tetrahydrate (Ca(NO₃)₂·4H₂O, Wenzhou Hengshun Chemical Co., Ltd), sodium bicarbonate (NaHCO₃, Tianjin Zhiyuan Chemical Reagent Co., Ltd), absolute alcohol (C₂H₅OH, Huadong Reagent Factory, Shenyang), and sodium hydroxide (NaOH, Liaoning Quanrui Reagent Co., Ltd) were all of analytical grade. Ultra-pure water was made freshly in 24 h in the laboratory. All the chemical reagents were used as supplied without further purification.

2.2. Fabrication of superhydrophobic Cu²⁺-loaded coupled DTPMPA-modified composite coating

Pre-treatment of the copper substrate. The pure copper (T2) and copper alloy (H62) samples were polished successively by abrasive paper of 800, 1000, 1200, and 2000 meshes to eliminate the oxidation films. Then, all of the samples were cleaned with anhydrous ethanol, and ultrasonically cleaned in ultra-pure water for 10 min to remove dirt and grease. After soaking in 1.0 mol L^{-1} HCl solution for 10 min, the samples were rinsed with a large amount of ultra-pure water to be neutral, and then put into an anhydrous ethanol solution for standby.

Firstly, the anode oxidation of H62 was illustrated in Fig. 1a. A traditional two-electrode system was employed for sample treatment with an H62 sheet as the anode and a T2 sheet as the cathode for electrolysis in a 3.0 mol L^{-1} KOH solution and magnetic stirring. The whole reaction proceeded by constant-current electrolysis at current density of 50 mA cm^{-2} and 55 °C for 6 min. After that, the anodized sample was cleaned by ultra-pure water and dried with a
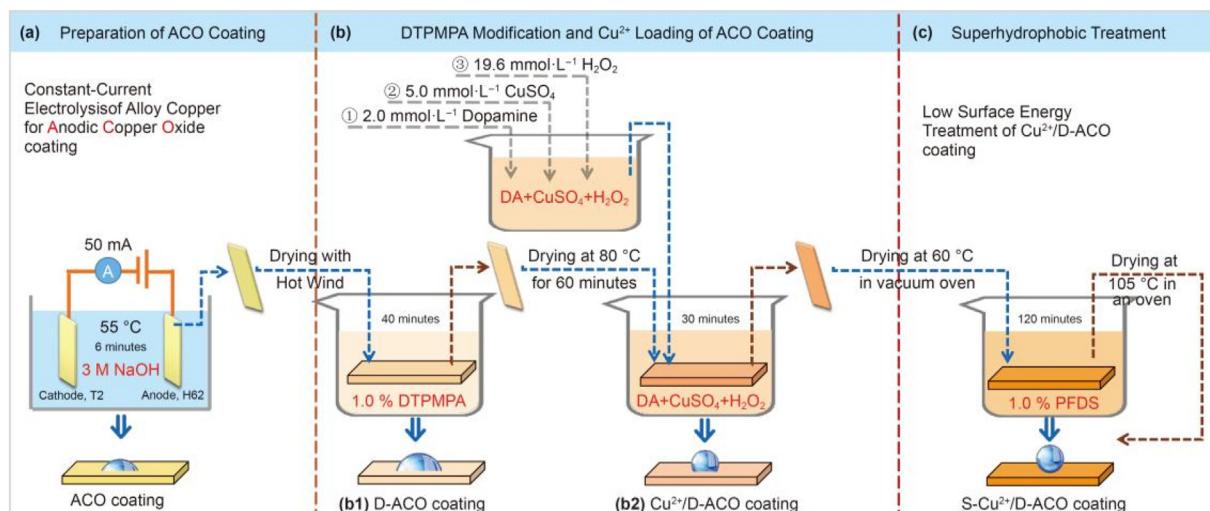
Fig. 1. Processing fabrication of ACO (**a**), Cu^{2+}/D-ACO (**b**), and S−Cu^{2+}/D-ACO (**c**) coatings.

hot air blower. The sample was marked as the anodized copper oxide (ACO) coating.

Secondly, DTPMPA modification and Cu^{2+} loading of the ACO coating were shown in Fig. 1b. The ACO coating was immersed into a 1.0 wt% DTPMPA solution for 40 min, and then dried in a vacuum oven at 80 °C for 60 min. The sample was marked as the DTPMPA-modified ACO (D-ACO) coating (Fig. 1b1). Then the 2.0 mg L^{-1} DA aqueous solution was dissolved in 20 mL of a Tris buffer (pH 8.5, 50 mmol L^{-1}). Next, 5 mmol L^{-1} $CuSO_4$ and 19.6 mmol L^{-1} H_2O_2 were added in turn under magnetic stirring to well dissolve the solution (Fig. 1b2). The D-ACO coating was fully wetted by anhydrous ethanol and immersed into the above deposition solution for 30 min at room temperature. The specimen was marked as the Cu^{2+}-loaded and DTPMPA-modified ACO (Cu^{2+}/D-ACO) coating (Fig. 1b2).

Thirdly, the superhydrophobic treatment of the Cu^{2+}/D-ACO coating was depicted in Fig. 1c. The sample was washed with ultra-pure water three times and dried at 60 °C in a vacuum oven until reaching constant weight. Afterwards, the treated sample was immersed into a 1.0 wt% PFDS ethanol solution for 2 h, and then oven-dried constantly at 100−105 °C for 1 h. The sample was named the superhydrophobic Cu^{2+}-loaded and DTPMPA-modified ACO (S−Cu^{2+}/D-ACO) coating (Fig. 1c).

2.3. CaCO_3 scaling at different coatings

Scale formation was carried out in a supersaturated $CaCO_3$ solution consisting of 0.06 mol L^{-1} $Ca(NO_3)_2 \cdot 4H_2O$ and 0.12 mol L^{-1} $NaHCO_3$ aqueous solutions (Eq. (1)). First, 750 mL $NaHCO_3$ solution (aq) was added into 750 mL $Ca(NO_3)_2 \cdot 4H_2O$ solution (aq) to form a suspension, which was adjusted to pH 11. Then the concentration of Ca^{2+} was monitored by an inductively coupled plasma atomic emission spectrometer (2100 DV, PerkinElmer). Calcium nitrate and sodium bicarbonate were added as needed, ensuring the concentrations of calcium and carbonate ions remained constant.

$$Ca(NO_3)_2 \cdot 4H_2O + 2NaHCO_3 \rightarrow CaCO_3 + 2NaNO_3 + 5H_2O + CO_2\uparrow \quad (1)$$

The H62, ACO, D-ACO, Cu^{2+}/D-ACO and S−Cu^{2+}/D-ACO coatings were immersed into the above solution separately. After that, the mixed solutions were heated constantly at 60 °C in a water bath. After certain time, the samples were gently removed from the supersaturated $CaCO_3$ solution, rinsed with ultra pure water, and then

dried at 100−105 °C. Each coating sample was tested three times, and the average value was taken as the scaling weight.

2.4. Characterization

Surface morphology and chemical elemental compositions of different coatings before and after scaling were examined by SEM (COXEM, EM-30AX) device equipped with energy dispersive spectrometer (EDS). Functional groups in the coatings were characterized by an FTIR spectroscope (Spectrum 2000; PerkinElmer) from 4000 to 450 cm^{-1}. Chemical composition and $CaCO_3$ crystalline structure were analyzed by XRD (PANalytical, PW3040/60, scanned from 20 to 100°). An ESCALAB 250Xi XPS meter equipped with a hemispherical analyzer was operated with Al Kα radiation (E = 1486.6 eV) and at a pass energy of 30 eV. Static water contact angle (WCA) of the coating was analyzed by an optical contact angle meter & interface tensiometer (SL200KS, USA KINO Industrial Ltd.).

3. Results and discussion

3.1. Characterization of coatings

3.1.1. Morphology analysis

The H62 (WCA = 93.94°) has relatively smooth surface, but polishing scratches can be observed after magnification (Fig. 2a). After the anodic oxidation, many micro-pores are formed at the surface of the ACO coating, which are beneficial for absorbing more water than that of H62, so the ACO coating has a hydrophilic surface with WCA of 14.97° (Fig. 2b). Meanwhile, the structure of micro-pores also provides place for absorbing DTPMPA and improves the anti-scaling of the ACO coating (Zhu et al., 2021b). For the D-ACO coating, the rough structure is obviously different from that of the ACO coating (Fig. 2c). Owing to the DTPMPA modification, the WCA of the D-ACO coating is 48.80°, which indicates hydrophilicity. After further modification with PDA under the promotion by Cu^{2+}, the Cu^{2+}/D-ACO coating becomes hydrophobic with WCA of 122.25° that founded on the micro-nano structure (Fig. 2d−d1). Finally, hydrophobic processing of PFDS coupled with the micro-nano structure of the Cu^{2+}/D-ACO coating produces the superhydrophobic S−Cu^{2+}/D-ACO coating with WCA of 163.03° (Fig. 2e).

3.1.2. FTIR spectra

The FTIR spectra of different coatings are shown in Fig. 3. For the
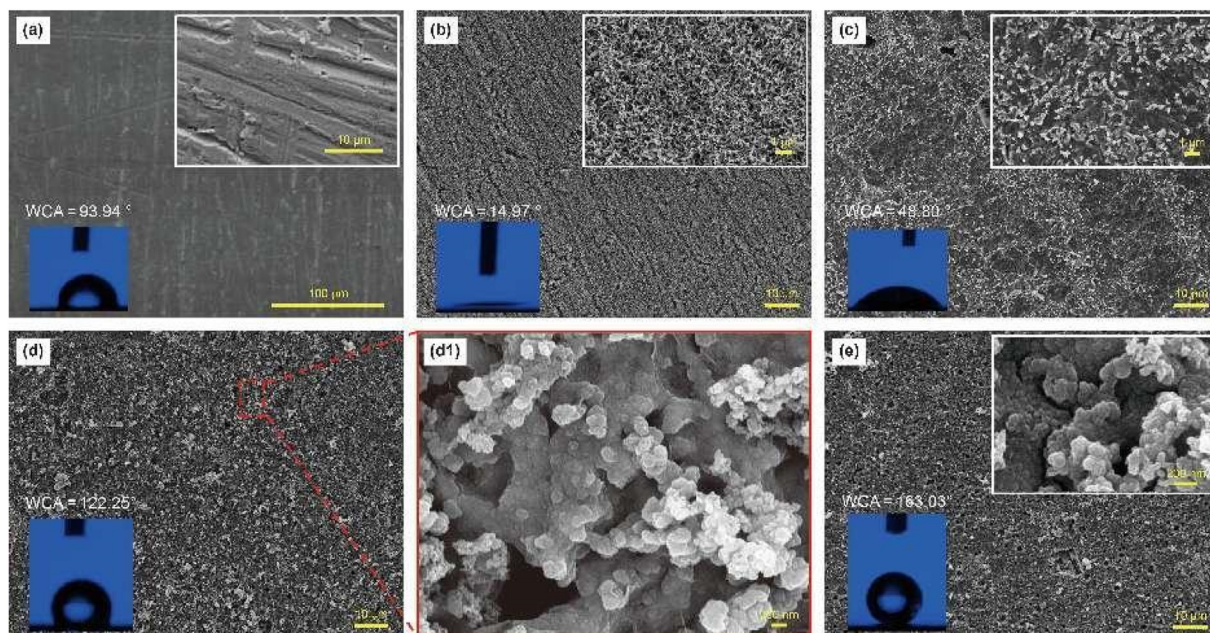
Fig. 2. SEM images of H62 (**a**), ACO (**b**), D-ACO (**c**), Cu^{2+}/D-ACO (**d, d1**), and S–Cu^{2+}/D-ACO (**e**) coatings.
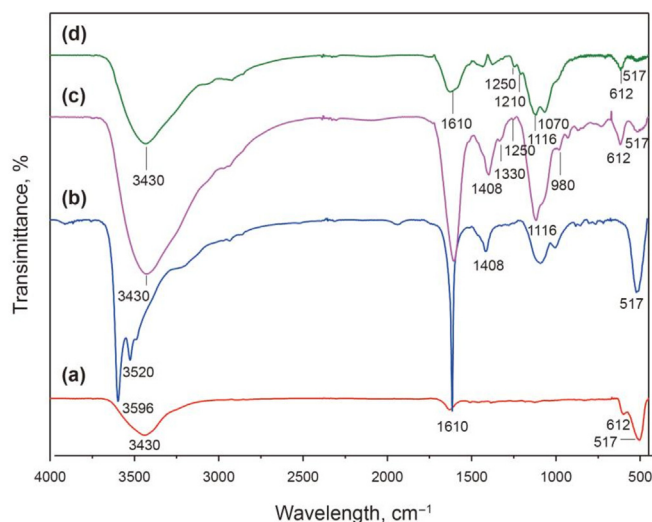
Fig. 3. FTIR spectra of ACO (**a**), D-ACO (**b**), Cu^{2+}/D-ACO (**c**) and S–Cu^{2+}/D-ACO (**d**) coatings.

ACO coating, the absorption band at 3430 cm^{-1} assigned to stretching vibration of O–H (Fig. 3a) is strengthened by the presence of the phenolic hydroxyl groups during autoxidation of DA in the D-ACO, Cu^{2+}/D-ACO and S–Cu^{2+}/D-ACO coatings (Fig. 3b–d). The band at 1610 cm^{-1} ascribed to carbonyl is very weak in the ACO coating because of the tiny amount (Fig. 3a), but is intensified sharply in the D-ACO, Cu^{2+}/D-ACO and S–Cu^{2+}/D-ACO coatings (Fig. 3b–d), owing to the modification of DTPMPA and PDA. For the D-ACO coating (Fig. 3b), the new sharp bands at 3596 and 3520 cm^{-1} are correlated to P–OH from DTPMPA. Besides, the bands at 612 and 517 cm^{-1} confirm the bending vibration of Cu–O–Cu in Cu$_2$O, and of Cu–O in CuO respectively (Zhang et al., 2020). Meanwhile, the new band at 1408 cm^{-1} in the D-ACO (Fig. 3b) coating and Cu^{2+}/D-ACO coating (Fig. 3c) corresponds to P–OH, indicating the successful adsorption of DTPMPA in the

coatings. Moreover, the band at 517 cm^{-1} is dramatically boosted after DTPMPA adsorption, which proves the formation of new co-ordination bonds (Fig. 3b). Specifically, a DTPMPA and Cu^{2+} chelate may be produced in the anodization of H62 to form DTPMPA:Cu^{2+} (Tozar and Karahan, 2014), and can chemically bond with the substrate. As for the Cu^{2+}/D-ACO coating, the band at 1408 cm^{-1} is intensified after the combination of the phenolic hydroxyl group from PDA (Fig. 3c). The new bands at 1330 and 1250 cm^{-1} are linked to the stretching vibration of C–N from the aromatic ring in PDA, and the strong band at 1116 cm^{-1} is characteristic of O–P–O (Fig. 3c). Further, the weak band at 980 cm^{-1} is ascribed to P–N–C, illustrating that –OH in DTPMPA reacts with –NH$_2$ in PDA (Fig. 3c). In comparison with the D-ACO coating (Fig. 3b), the band at 1610 cm^{-1} of the Cu^{2+}/D-ACO coating (Fig. 3c) is weakened evidently in intensity, demonstrating that the consumption of
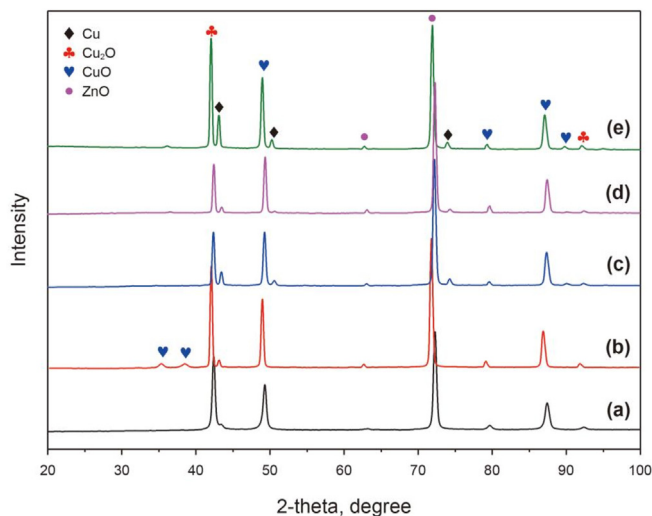
Fig. 4. XRD spectra of H62 (**a**), ACO (**b**), D-ACO (**c**), Cu^{2+}/D-ACO (**d**), and S–Cu^{2+}/D-ACO (**e**) coatings.

carbonyl (C=O) during the DTPMPA and PDA reaction. With regard to the S–Cu^{2+}/D-ACO coating, the weak band at 1210 cm^{-1} is associated with the asymmetric stretching vibration of CF$_2$ in PFDS and 1070 cm^{-1} of Si–O–Si, respectively (Fig. 3d), suggests the PFDS cross-linked and formed the superhydrophobic coating (Fig. 3d).

3.1.3. XRD results

XRD patterns of the five coatings are shown in Fig. 4. For all the samples, the peaks at 43.3, 50.4, 74.1, 42.3, 92.4, 49.2, 79.8, 87.1 and 89.8° are assigned to the (111), (200), (220) planes of Cu, (200) and (400) planes of Cu$_2$O (Cardiano et al., 2017), and (202), (023), (114), and (131) planes of CuO, respectively (Choi et al., 2016). There are also characteristic peaks of CuO at 35.5° (002), 38.7° (111), and ZnO at 62.7° (103), 72.3° (004). Compared with the original copper alloy H62 (Fig. 4a), the peaks at 42.3, 49.2, and 72.3° of the ACO coating are all considerably enhanced in intensity, demonstrating that the formation of Cu$_2$O, CuO, and ZnO (Fig. 4b). For the D-ACO coating (Fig. 4c), the peak intensities of Cu$_2$O (43.3°) and CuO (49.2°) are both decreased after DTPMPA modification of the ACO coating, which is caused by chemical reactions between DTPMPA with Cu$_2$O and CuO (Cardiano et al., 2017). Moreover, owing to the reaction between PDA and Cu^{2+} (from CuSO$_4$), the peak strength of CuO is slightly higher than that of Cu$_2$O in the Cu^{2+}/D-ACO (Fig. 4d), so that Cu^{2+} can be loaded in the coating. With regard to the S–Cu^{2+}/D-ACO coating (Fig. 4e), little is altered in the peak area of Cu$_2$O or CuO, which is because hydrophobic processing will not change the crystalline state or composition of coatings.

3.1.4. XPS spectra

The Cu 2p core level spectrum of the S–Cu^{2+}/D-ACO coating can be split into two groups of peaks with a spin-orbit splitting energy of ~20.07 eV (Fig. 5a). Specifically, the peaks at 953.13 eV (Cu 2p$_{1/2}$) and 933.06 eV (Cu 2p$_{3/2}$) accredit the presence of Cu$_2$O, and the peaks at 954.68 (Cu 2p$_{1/2}$) and 934.61 eV (Cu 2p$_{3/2}$) reflect the presence of CuO. The corresponding quantitative calculation shows that the area ratio between Cu$^+$ and Cu^{2+} in the S–Cu^{2+}/D-ACO coating is about 1:9 (Table S1), which means the copper is mainly divalent (Cu^{2+}). Meanwhile, the satellite peaks from CuO at 962.45, 943.67 and 941.42 eV further prove its existence in the S–Cu^{2+}/D-ACO coating (Fig. 5a). Furthermore, the peak at 937.30 eV related to Cu 2p$_{1/2}$ deviates obviously from the theoretical value of 933.70 eV (Gonzalez et al., 1996), owing to the charge effect caused by coordination between DTPMPA and copper ions, which directly reveals the occurrence of chelation in the fabrication of the S–Cu^{2+}/D-ACO

coating. Moreover, the O1s XPS spectrum of the S–Cu^{2+}/D-ACO coating (Fig. 5b) shows peaks at 529.90, 530.60, and 531.10 eV that are attributed to O–Cu, Cu–O–Cu, and O–Zn respectively, and a peak at 531.90 eV is assigned to the C–OH in DTPMPA and PDA.

3.2. CaCO$_3$ scaling of S–Cu^{2+}/D-ACO coating

To clarify the anti-scaling performance of different coatings, we carried out static deposition experiments in a supersaturated CaCO$_3$ solution at 60 °C, and calculated the mass differences. In the process of CaCO$_3$ deposition, the variation of CaCO$_3$ scaling rates at different coatings with immersion time can be divided into three stages (Fig. 6). In the first stage (from 0 to 10 h), the average CaCO$_3$ scaling rates at the H62, ACO, D-ACO, Cu^{2+}/D-ACO, and S–Cu^{2+}/D-ACO coatings are 0.0080, 0.0092, 0.0060, 0.0042, and 0.0030 mg/ (cm^2·h), respectively. The scaling rate of the ACO coating is the highest (Fig. 6b) and the S–Cu^{2+}/D-ACO coating is the lowest (Fig. 6e). In the second stage (from 10 to 24 h), the CaCO$_3$ scaling rates of the above coatings are 0.0009, 0.0023, 0.0014, 0.0017 and 0.0015 mg/(cm^2·h), respectively. In the third stage (from 24 to 48 h), the scaling rates of these coatings stabilize at 0.0006, 0.0003, 0.0004, 0.0002 and 0.0003 mg/(cm^2·h) respectively. In the whole period of CaCO$_3$ scaling, the scale masses of the H62, ACO, D-ACO,
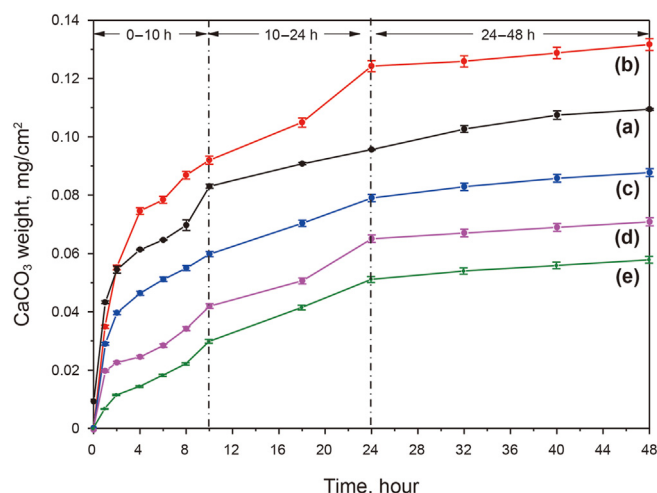
Fig. 6. Variations of CaCO$_3$ scaling weight with immersion time at the surface of H62 (**a**), ACO (**b**), D-ACO (**c**), Cu^{2+}/D-ACO (**d**), and S–Cu^{2+}/D-ACO (**e**) coating.
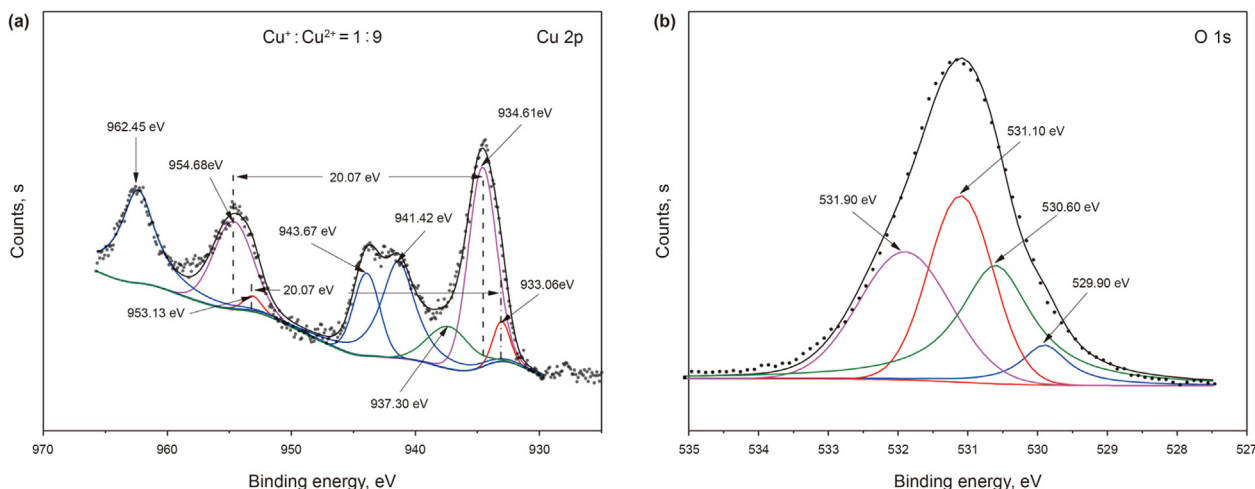
Fig. 5. Cu 2p (**a**) and O 1s (**b**) XPS spectra of the S–Cu^{2+}/D-ACO coating.

Cu^{2+}/D-ACO and S−Cu^{2+}/D-ACO coatings are 0.1075, 0.1313, 0.1075, 0.0878, 0.0705, and 0.0579 mg/cm^2 respectively. The scale mass at the S−Cu^{2+}/D-ACO coating is only 44.1% that of the ACO coating after soaking in superssaturated $CaCO_3$ solution for 48 h. The above results demonstrate that the S−Cu^{2+}/D-ACO coating displays outstanding anti-scaling performance.

3.3. Analysis of $CaCO_3$ scaling at various coatings

3.3.1. $CaCO_3$ scaling deposition at different coatings

The effect of coating surface on scale deposition was assessed by morphological, functional groups and phase analyses of $CaCO_3$ scaling. The deposited $CaCO_3$ exhibits cubic, rod-like, thin plate-like, or needle-like crystals on above coatings' surface after immersion in the supersaturated $CaCO_3$ solution for 10 h. Moreover, the size of cubic crystals ranges from 3 to 12 μm and the length of the rod/needle-like crystals is 10−15 μm (Fig. 7). For the H62 (Fig. 7a), a large amount of $CaCO_3$ particles deposit at the surface and partially form obvious cube crystals, which even grew to crystal twins in length of ~75 μm. However, fewer cubes exist at the ACO coating surface compared with H62, and are placed by some needle-like crystals, with 8-μm-long separate cubes (Fig. 7b). With regard to the D-ACO coating and the Cu^{2+}/D-ACO coating, $CaCO_3$ scale mainly appears as acicular and less cubic crystals (Fig. 7c− d). Furthermore, very few $CaCO_3$ crystals deposit at the S−Cu^{2+}/D-ACO coating surface, and only a tiny amount of cubes in length of about 3−5 μm are formed (Fig. 7e). Therefore, the DTPMPA existing at the interface between the supersaturated $CaCO_3$ solution and the S−Cu^{2+}/D-ACO coating surface conspicuously affects the morphology and size of the $CaCO_3$ crystals (Chen et al., 2019).

The FTIR spectra of $CaCO_3$ scaling at different coatings after 10 h are shown in Fig. 8. There is a similarly situation of H62 (Fig. 8a) and ACO (Fig. 8b), they all show bands at 3430 and 1632 cm^{-1} of stretching vibrations of O−H and C═O, a strong band at 1388 cm^{-1} of asymmetric stretching vibration of C−O for calcite, a weak band at 612 cm^{-1} of Cu_2O (Zhang et al., 2020), and a wide band at 505 cm^{-1} of ZnO. For the $CaCO_3$ scaling at surface of the D-ACO coating, the new band at 1250 cm^{-1} reflects the C−N vibration of
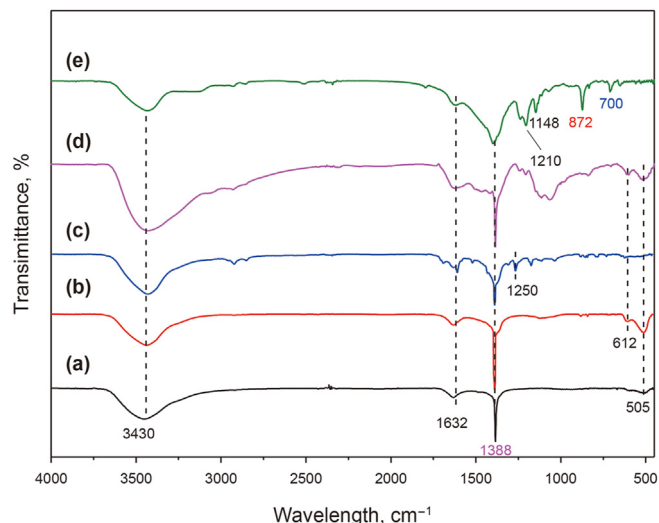
Fig. 8. FTIR spectra of $CaCO_3$ scaling at the surface of the H62 (**a**), ACO (**b**), D-ACO (**c**), Cu^{2+}/D-ACO (**d**), and S−Cu^{2+}/D-ACO (**e**) coatings after soaking in the supersaturated $CaCO_3$ solution for 10 h.

aromatic ring in DTPMPA (Fig. 8c). In comparison with the D-ACO coating (Fig. 8c), the $CaCO_3$ scale deposited at the Cu^{2+}/D-ACO coating surface shows a stronger vibration of C−O for calcite at 1388 cm^{-1}, owing to the interference of Cu^{2+} and DTPMPA to $CaCO_3$ scaling deposition (Fig. 9d). For the S−Cu^{2+}/D-ACO coating (Fig. 8e), the weak bands at 1210 and 1148 cm^{-1} are correlated to the stretching vibration of CF_2 and CF_3 in PFDS, respectively. Besides, the obvious band at 872 cm^{-1} confirms the presence of vaterite $CaCO_3$ scale, and the new band at 700 cm^{-1} is assigned to the in-plane bending of aragonite (Fig. 8e) (Niu et al., 2014).

The XRD spectra of $CaCO_3$ scaling at different coatings are shown in Fig. 9. The crystal phase of $CaCO_3$ after 10 h deposition at the surface of H62, ACO, D-ACO, Cu^{2+}/D-ACO, and S−Cu^{2+}/D-ACO coating is polymorphs, which mainly consist of calcite and
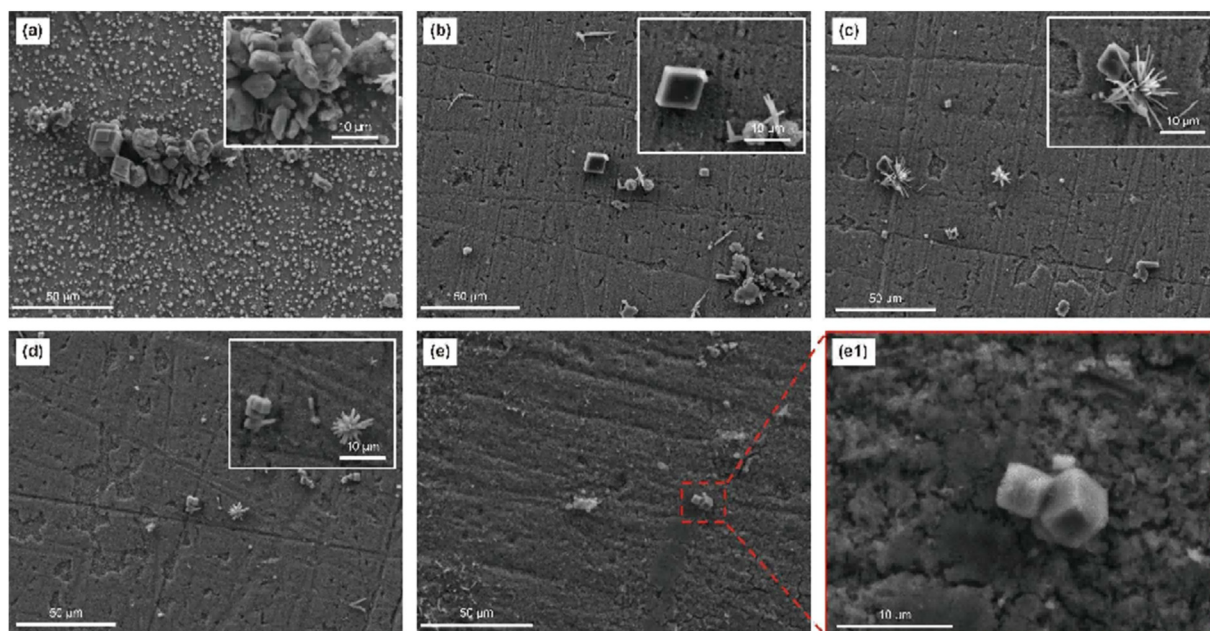
Fig. 7. SEM images of $CaCO_3$ scaling at the surface of H62 (**a**), ACO (**b**), D-ACO (**c**), Cu^{2+}/D-ACO (**d**), and S−Cu^{2+}/D-ACO (**e, e1**) coatings after immersion for 10 h.
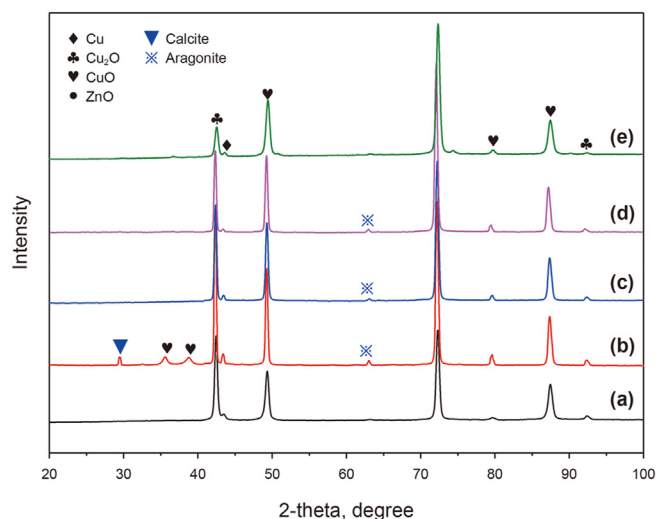
Fig. 9. XRD of CaCO₃ scaling at the surface of H62 (**a**), ACO (**b**), D-ACO (**c**), Cu²⁺/D-ACO (**d**) and S−Cu²⁺/D-ACO (**e**) coatings after immersion in the supersaturated CaCO₃ solution for 10 h.

aragonite at 29.5 and 62.9° (Fig. 9). There is hardly any CaCO₃ scale at the H62 surface (Fig. 9a). Moreover, the peak intensity of calcite (29.5°) at the ACO coating surface (Fig. 9b) is dramatically stronger than that of other coatings, which is basically consistent with the trend of surface scaling mass at different coatings (Fig. 6). For the D-ACO coating (Fig. 9c) and the Cu²⁺/D-ACO coating (Fig. 9d), the peak of aragonite (62.9°) CaCO₃ scale is observed, but in low intensity. Actually, aragonite is less stable than calcite, which means the CaCO₃ scale can escape from the D-ACO coating and the Cu²⁺/D-ACO coating surface. As for the S−Cu²⁺/D-ACO coating (Fig. 9e), there is no peak for CaCO₃ scale, which reflects high scaling resistance.

3.3.2. Deposition of CaCO₃ scaling at the S−Cu²⁺/D-ACO coating surface

To investigate the deposition process of CaCO₃ at the surface of the S−Cu²⁺/D-ACO coating, we analyzed the morphology of the scale after different times' soaking. Only a tiny amount of spherical CaCO₃ scale in diameter of ~4.0 μm deposits at the interface after immersion for 1 h (Fig. 10a-10a1). With the extension of scaling time to 18 h, the amount of spherical CaCO₃ scale in diameter of ~5.0 μm increases obviously (Fig. 10b), and different shapes appear, such as cube and other irregular shapes (Fig. 10b1). When the immersion time prolongs to 24 h, abundant CaCO₃ scale can be seen at

the S−Cu²⁺/D-ACO coating surface (Fig. 10c−c1). Moreover, multiple shapes coexist, including sphere, cube and even trapezoid prism (Fig. 10c), and the spherical and cubic crystals are interspersed to form a coherent in total size of ~30 μm (Fig. 10c1). The results prove that the CaCO₃ scale at the S−Cu²⁺/D-ACO coating surface tends to be increasingly stable with the prolonging of soaking time. The XRD analysis of CaCO₃ deposits at S−Cu²⁺/D-ACO coating surface at different periods (Fig. S1) demonstrate that although more CaCO₃ scale is attached to the coating surface, the XRD intensity of CaCO₃ scale for 24 h is very weak, that is, the absolute quantity is very small.

3.4. Mechanistic analysis of the S−Cu²⁺/D-ACO coating fabrication

As we all know, the properties of materials depend on the molecular structure and composition of materials. For the S−Cu²⁺/D-ACO coating, the electrochemical oxidation of the copper alloy and the modification of DTPMPA and Cu²⁺ determine that it has excellent anti-scaling performance.

Firstly, the reaction of copper alloy (H62) oxidized to anodized copper oxide (ACO) to form porous structure, the reaction equations are:

$$2Cu + 2OH^- \rightarrow Cu_2O + H_2O + 2e^- \tag{2}$$

$$Cu_2O + 2OH^- \rightarrow 2CuO + H_2O + 2e^- \tag{3}$$

$$Zn + 2OH^- \rightarrow ZnO + H_2O + 2e^- \tag{4}$$
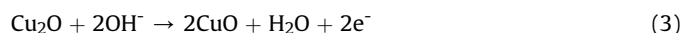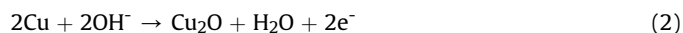
Secondly, the equations of DTPMPA modification and Cu²⁺ loading are:

$$DTPMPA + 2H^+ + CuO \rightarrow DTPMPA{:}Cu^{2+} + H_2O \tag{5}$$

$$2DTPMPA + 2H^+ + Cu_2O \rightarrow 2DTPMPA{:}Cu^+ + H_2O \tag{6}$$

In these two parts, the main reactions, including the formation of CuO (reactions (2) and (3)) and the formation of DTPMPA:Cu²⁺ (reaction (5)), ensure that DTPMPA can be closely combined with the substrate ACO through chemical bond, and can be effectively stored in the micro-porous structure of the S−Cu²⁺/D-ACO coating.

Thirdly, PFDS and PDA modification of the anodized copper oxide and superhydrophobic processing are:

Through reactions (7) and (8), on the one hand, the chemical reaction among PDA, DTPMPA and CuSO₄ realizes the loading of Cu²⁺ at the interface of the S−Cu²⁺/D-ACO coating. On the other hand, the S−Cu²⁺/D-ACO coating gains superhydrophobicity after modified by the low surface energy substance PFDS.

(7)
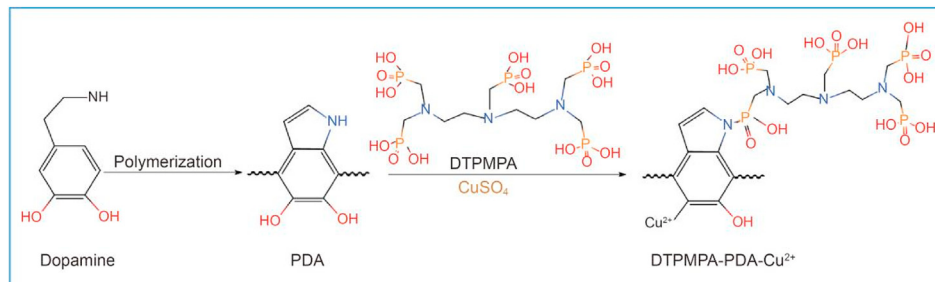
Chelating reaction of dopamine with Cu²⁺ ion
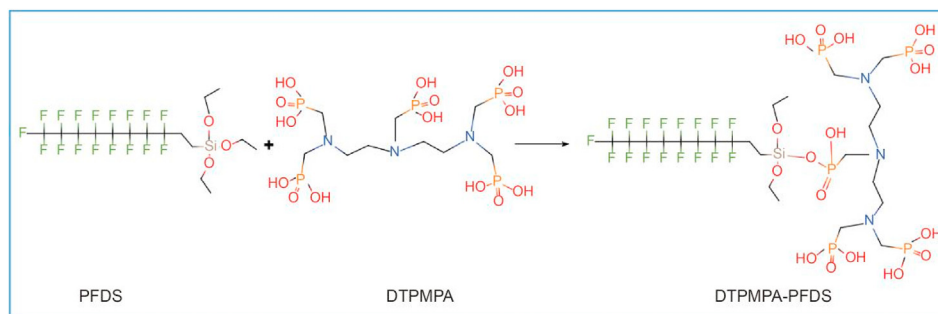
(8)

Chemical reaction between PFDS and DTPMPA

3.5. Mechanism of scale deposition at the S−Cu^{2+}/D-ACO coating

The anti-scaling performance of superhydrophobic coating and the dynamic scale prohibition was reported before (Qian et al., 2017; Zhu et al., 2021b). Herein, for the S−Cu^{2+}/D-ACO coating,

its unique scale prohibition can be explained from three aspects: superhydrophobicity, dynamic release of DTPMPA, and the inhibition of Cu^{2+} on CaCO$_3$ scaling (Fig. 11).

First, as for the superhydrophobic scale inhibition, an obvious air layer exists between the S−Cu^{2+}/D-ACO coating (WCA of 163.03°,
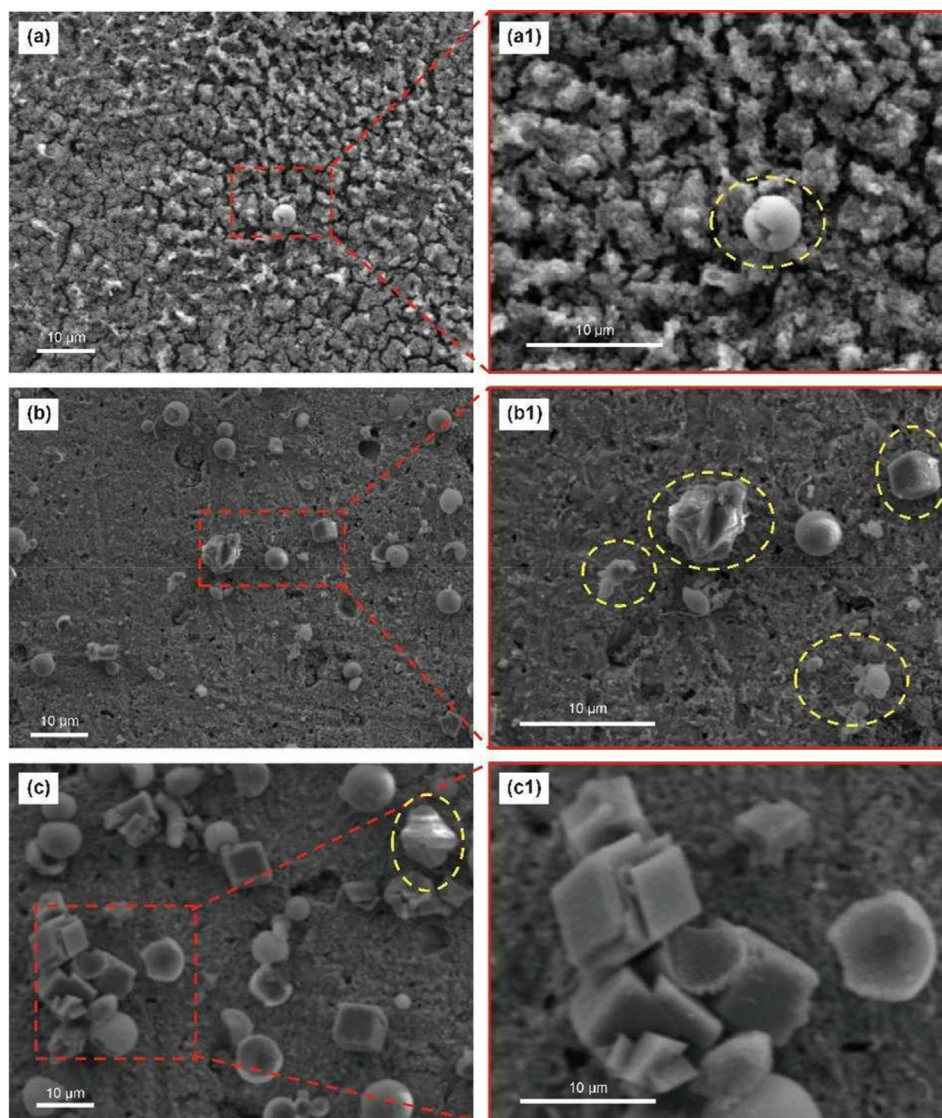
Fig. 10. SEM images of CaCO$_3$ scaling at the surface of S−Cu$_{2+}$/D-ACO coating after different time's immersion: 1 h (**a, a1**), 18 h (**b, b1**), and 24 h (**c, c1**).

Fig. 2e) and the supersaturated CaCO$_3$ solution, which is different from the other three surfaces and results in a small liquid-solid contact area and an initial wetting behavior of the Cassie-Baxter state (Cassie and Baxter, 1944). Accordingly, the crystalline area of water-solid interface is reduced, which improves the anti-scaling performance of the S−Cu^{2+}/D-ACO coating (Qian et al., 2017). Relevant studies show that heterogeneous nucleation at the water-solid interface is usually more favorable than homogeneous nucleation. The Gibbs free energy of heterogeneous nucleation at the water-gas interface is equivalent to that of homogeneous nucleation (Kashchiev and Firoozabadi, 2002). Because the surface free energy is almost zero in air and is low in PFDS, the S−Cu^{2+}/D-ACO coating has the lowest scaling propensity in protecting the air layer (Fig. S2d1) than other coatings (Fig. S2a1-S2c1).

Second, the role of DTPMPA at the interface is important. During the fabrication of the S−Cu^{2+}/D-ACO coating, DTPMPA can chemically bond with Cu^{2+} to form DTPMPA:Cu^{2+}, which ensures its tight adsorption with the substrate (Fig. 3) and makes it lurk in the micro-structure of the coating. This is like being "locked" in the substrate (Fig. 12a), which enables DTPMPA to be stored in the coating. When the S−Cu^{2+}/D-ACO coating is exposed to the supersaturated CaCO$_3$ solution, DTPMPA will be released and chelate with Ca^{2+} to form DTPMPA:Ca^{2+} at the interface between the CaCO$_3$ solution and the S−Cu^{2+}/D-ACO coating (Fig. 12b). The full survey XPS spectra of the S−Cu^{2+}/D-ACO coating after CaCO$_3$ scaling for 10 h show a new peak at about 347.50 eV (Fig. 13a) that corresponds to Ca 2p, which reveals the Ca^{2+} depositing at the S−Cu^{2+}/D-ACO coating surface in form of DTPMPA:Ca^{2+}. According to the hard and soft acids and bases theory (HSAB) (Pearson, 1963), Ca^{2+}, Cu^{2+} and DTPMPA belong to hard acid, borderline acid and hard base, respectively. In general, hard acids tend to bind with hard bases, and soft acids tend to bind with soft bases. In addition, the coordination ions formed by boundary acids and hard bases or soft bases are not very stable. Consequently, the DTPMPA:Cu^{2+} and
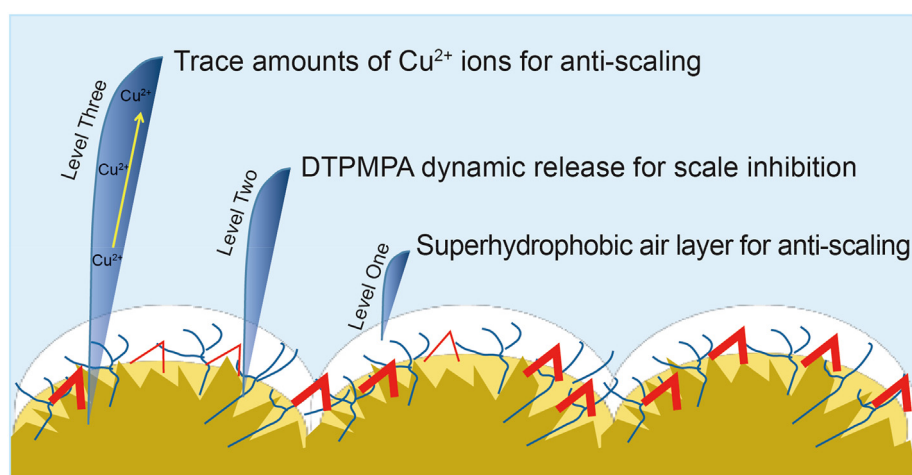
Fig. 11. The coupling effect for anti-scaling of the S−Cu^{2+}/D-ACO coating.
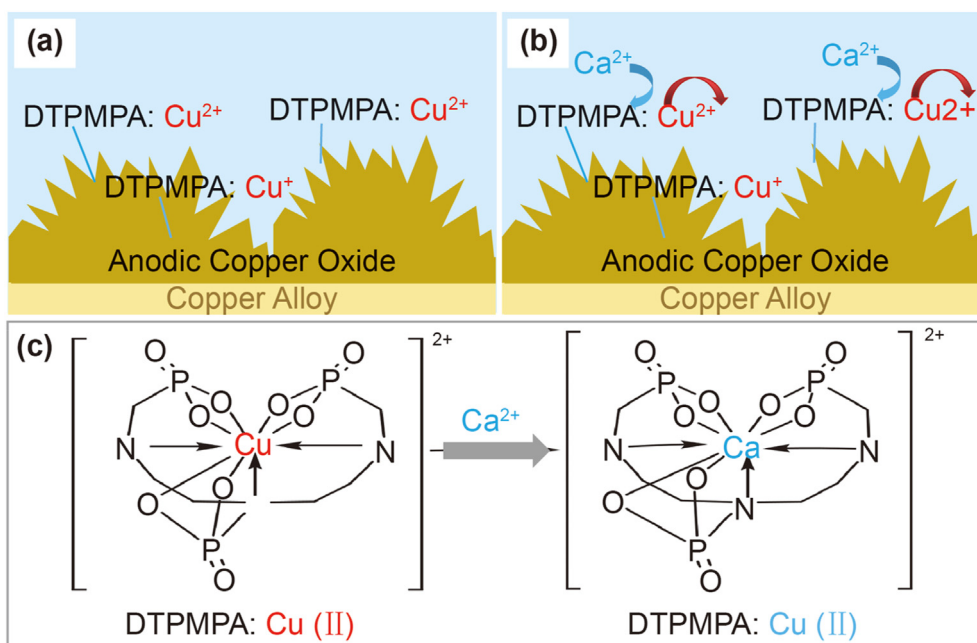
Fig. 12. Schematic diagram of chemical bonding between Cu^{2+} and DTPMPA (**a**); ion exchange reaction (**b**) and chelate transformation (**c**) between Cu^{2+} and Ca^{2+} at the coating/solution interface.
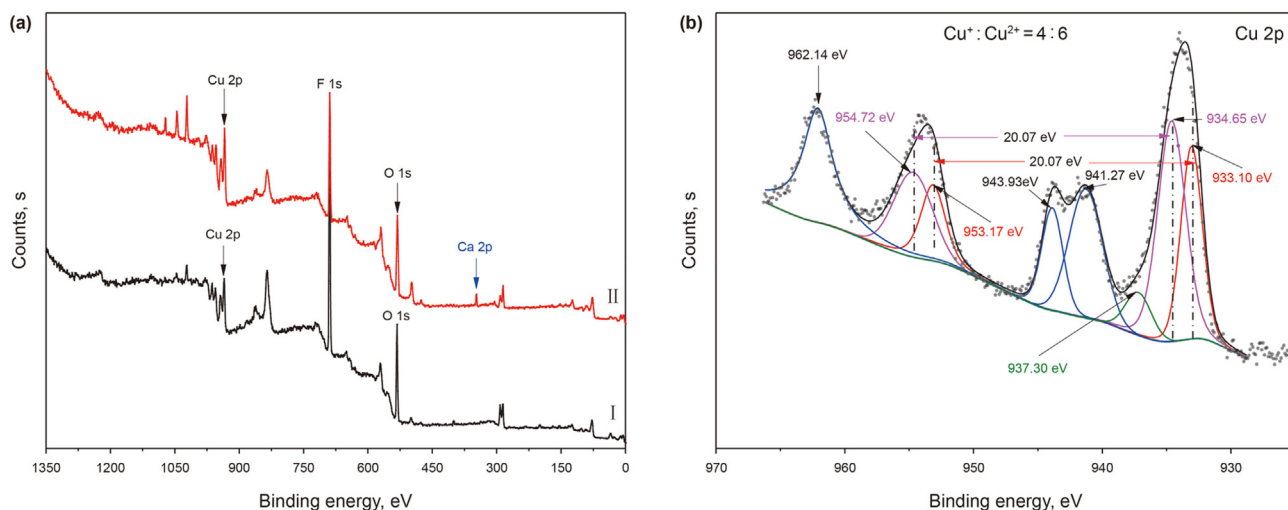
Fig. 13. XPS spectra of the S−Cu^{2+}/D-ACO coating (**a**-I) after 10 h immersion in the supersaturated CaCO$_3$ solution (**a**-II) and Cu 2p (**b**).
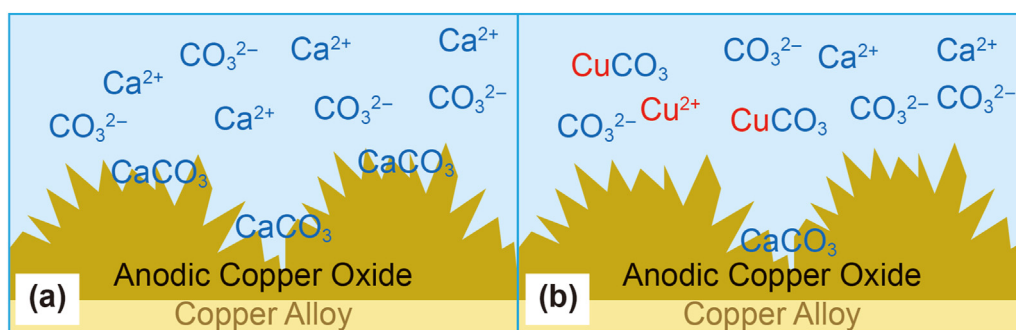
Fig. 14. Schematic diagram of Cu^{2+} ions anti-scaling mechanism of the S−Cu^{2+}/D-ACO coating.

Ca^{2+} would undergo an ion replacement reaction (Fig. 12c) to form DTPMPA:Ca^{2+} and Cu^{2+} during the deposition of CaCO$_3$ (Fig. 12c), the decreases of divalent copper (CuO, Table S1) in the S−Cu^{2+}/D-ACO coating and increases of Cu^{2+} in the supersaturated CaCO$_3$ solution (Table S2) have proved this point. The formation of DTPMPA:Ca^{2+} would not only prevent the combination of Ca^{2+} and CO$_3^{2-}$, but also induce the lattice distortion of CaCO$_3$ (Zhu et al., 2021b), all of which determine the good anti-scaling of the S−Cu^{2+}/D-ACO coating.

Third and the most importantly, Cu^{2+} plays a critical role in the anti-scaling of the S−Cu^{2+}/D-ACO coating. After CaCO$_3$ scaling for 10 h, the content of monovalent copper (Cu$_2$O) and divalent copper (CuO, Table S1) in the S−Cu^{2+}/D-ACO coating changed significantly. As shown of the Cu 2p XPS spectrum in Fig. 13b, the area ratio between the peaks of Cu$^+$ at 953.17 eV (Cu 2p$_{1/2}$) and 933.10 eV (Cu 2p$_{3/2}$), and Cu^{2+} at 954.72 eV (Cu 2p$_{1/2}$) and 934.65 eV (Cu 2p$_{3/2}$) is 4:6 in the S−Cu^{2+}/D-ACO coating after scaling (Fig. 13b, and Table S2). In comparison with the Cu 2p spectrum of the Cu^{2+}/D-ACO coating without scaling (Fig. 5a), the content of Cu^{2+} decreases and the Cu$^+$ increases, which indicates part of Cu^{2+} has released into the solution (Table S2). At the same time, many studies on the Cu^{2+} ion scaling inhibition show it is a very effective inhibitor at low concentration (Liu et al., 2011; Parsiegla and Katz, 2000; Zeppenfele, 2000). The anti-scaling effect of Cu^{2+} can be explained by the co-precipitation mechanism (Benslimane et al., 2020; Sabzi and Arefifinia, 2019). From the thermodynamic point of view, when the activity of Ca^{2+} and CO$_3^{2-}$ in the solution exceeds the saturation limit, CaCO$_3$ precipitation is possible (Fig. 14a) (Al-Roomi and

Hussain, 2016). However, the complexation of the released Cu^{2+} with carbonate ions is the most serious in a carbonate solution (Lin and Singer, 2005), and form the complex CuCO$_3$ (aq) (Fig. 14a), which inhibits the combination of Ca^{2+} and CO$_3^{2-}$. Therefore, the CuCO$_3$ (aq) complex will block the active growth in CaCO$_3$ nuclei and crystals formation (Fig. 14b), and results in a reduced scaling rate (Fig. 6). This is basically consistent with another study (Ghizellaoui et al., 2007). The inhibiting effect of Cu^{2+} leads to the formation of the mixed carbonate Cu$_x$Ca$_{1-x}$CO$_3$ in the solution, which effectively hinders the deposition of CaCO$_3$ at the S−Cu^{2+}/D-ACO coating (Liu et al., 2011).

Moreover, the elemental composition of CaCO$_3$ crystals at the surface of the S−Cu^{2+}/D-ACO coating was studied by EDS. The S−Cu^{2+}/D-ACO coating is mainly composed of Cu (70.21 wt%), C, O, F, P, and Zn (Table S3). This result is in good agreement with the XRD analysis (Fig. 4) that the coating is mainly composed of CuO and Cu$_2$O.

Compared with the S−Cu^{2+}/D-ACO coating, the content of Ca increases with the extension of scaling time and reaches 40.56 wt% and 42.26 wt% after scaling for 10 h and 24 h (Table S3), respectively. At the same time, the content of C and O elements belonging to carbonate also increases with the immersion time, suggesting the formation of CaCO$_3$ scale at the S−Cu^{2+}/D-ACO coating surface. In addition, the slight drop of P content in the coating indicates that DTPMPA is released from the S−Cu^{2+}/D-ACO coating into the solution. Furthermore, the content of Cu in the coating decreases significantly (Table S3), meanwhile the content of Cu^{2+} in the solution increases obviously (Table S2), which further confirms the

Cu^{2+} released from the S−Cu^{2+}/D-ACO coating to the supersaturated $CaCO_3$ solution. It's thanks to the react of the above released Cu^{2+} and CO_3^{2-} (Lin and Singer, 2005), the binding of Ca^{2+} and CO_3^{2-} would be inhibited that resulting in the decrease of $CaCO_3$ scaling. In all, based on the synergistic effect of dynamic release of DTPMPA at the liquid/solid interface, and the Cu^{2+} inhibition, the binding probability between Ca^{2+} and CO_3^{2-} is reduced, which endows the S−Cu^{2+}/D-ACO coating with outstanding anti-scaling performance. This work of the S−Cu^{2+}/D-ACO coating provides a new exploration and method for the scale inhibition in oilfield and relevant industries.

4. Conclusions

A novel DTPMPA-modified and Cu^{2+}-loaded anodized copper oxide (S−Cu^{2+}/D-ACO) superhydrophobic coating was fabricated for the first time, and its anti-scaling performance in a supersaturated $CaCO_3$ solution was studied in detail. In the scaling process, the superhydrophobic S−Cu^{2+}/D-ACO coating can retain a large air layer at the solution/coating interface, which is instrumental in preventing the formation and deposition of $CaCO_3$. In addition, the anti-scaling of the S−Cu^{2+}/D-ACO coating is a dynamic process: DTPMPA can be transferred from DTPMPA:Cu^{2+} (produced in coating fabrication) to DTPMPA:Ca^{2+}, which is a dynamic release of the scale inhibitor and prevents the reaction of Ca^{2+} and CO_3^{2-}. Most surprisingly, the inhibition of Cu^{2+} plays an important role in preventing the $CaCO_3$ deposition at the S−Cu^{2+}/D-ACO coating surface. The synergistic effect among the air layer retained in the coating/solution interface, the latent storage and dynamic release of DTPMPA, and the inhibition of Cu^{2+} on the deposition of $CaCO_3$ guarantees the outstanding anti-scaling performance of the S−Cu^{2+}/D-ACO coating. This study supplies a new method to fabricate an intelligent and efficient anti-scaling superhydrophobic surface, which is desired in scale inhibition in petroleum industry.

Appendix A. Supplementary data

Supplementary data to this article can be found online at https://doi.org/10.1016/j.petsci.2022.07.005.

References

Al-Roomi, Y.M., Hussain, K.F., 2016. Potential kinetic model for scaling and scale inhibition mechanism. Desalination 393, 18–195. https://doi.org/10.1016/j.desal.2015.07.025.

An, X.K., Yang, C., Wu, Z.Z., et al., 2020. Self-regulated super-hydrophobic Cu/CuO electrode film deposited by one-step high-power sputtering. Adv Electron Mater 6, 1900891–1900897. https://doi.org/10.1002/aelm.201900891.

Benslimane, S., Bouhidel, K.E., Ferfache, A., et al., 2020. Mechanistic study of the synergetic inhibiting effects of Zn^{2+}, Cu^{2+} and Mg^{2+} ions on calcium carbonate precipitation. Water Res. 186, 116323–116332. https://doi.org/10.1016/j.watres.2020.116323.

Cardiano, P., Cigala, R.M., Cordaro, M., et al., 2017. On the complexation of metal cations by "Pure" diethylenetriamine-N,N,N',N'',N''-pentakis-(methylenephosphonic) acid. New J. Chem. 41 (10), 4065–4075.. https://doi.org/10.1039/C7NJ00118E.

Cassie, A.B.D., Baxter, S., 1944. Wettability of porous surfaces. Trans. Faraday Soc. 40, 546–551. https://doi.org/10.1039/tf9444000546.

Chen, X.X., Wang, H.Y., Wang, C.J., et al., 2019. A novel antiscaling and anti-corrosive polymer-based functional coating. J. Taiwan Inst. Chem. Eng. 97, 397–405. https://doi.org/10.1016/j.jtice.2019.01.016.

Choi, J., Oh, H., Han, S.W., et al., 2016. Preparation and characterization of graphene oxide supported Cu, Cu_2O, and CuO nanocomposites and their high photocatalytic activity for organic dye molecule. Curr. Appl. Phys. 17, 137–145. https://doi.org/10.1016/j.cap.2016.11.020.

Dong, X.J., Meng, J.B., Hu, Y.Z., et al., 2020. Fabrication of self-cleaning superhydrophobic surfaces with improved corrosion resistance on 6061 aluminum alloys. Micromachines 11 (2), 159–172. https://doi.org/10.3390/mi11020159.

Dou, J., Huang, Q., Huang, H.Y., et al., 2019. Mussel-inspired preparation of layered double hydroxides based polymer composites for removal of copper ions. J. Colloid Interface Sci. 533, 416–427. https://doi.org/10.1016/j.jcis.2018.08.064.

Edvardsen, L., Gawel, K., Wenner, S., et al., 2020. Electrochemical enhancement and inhibition of calcium carbonate deposition. J. Environ. Chem. Eng. 8 (5), 104239. https://doi.org/10.1016/j.jece.2020.104239.

Feng, L.B., Yan, Z.N., Shi, X.T., et al., 2018. Anti-icing/frosting and self-cleaning performance of superhydrophobic aluminum alloys. Appl. Phys. 124 (2), 142–155. https://doi.org/10.1007/s00339-017-1509-x.

Ghizellaoui, S., Euvrad, M., Ledion, J., et al., 2007. Inhibition of scaling in the presence of cooper and zinc by various chemical processes. Desalination 206 (1–3), 185–197. https://doi.org/10.1016/j.desal.2006.02.066.

Ghosh, B., Sun, L.Y., Thomas, N.C., 2019. Compatibility evaluation of modified seawater for EOR in carbonate reservoirs through the introduction of polyphosphate compound. Petrol. Sci. 17 (12), 393–408. https://doi.org/10.1007/s12182-019-00380-6.

Gonzalez, Y., Lafont, M.C., Pebere, N., et al., 1996. A synergistic effect between zinc salt and phosphonic acid for corrosion inhibition of a carbon steel. J. Appl. Electrochem. 26, 1259–1265. https://doi.org/10.1007/BF00249928.

Guo, M.M., Liu, M.L., Zhao, W., et al., 2015. Rapid fabrication of SERS substrate and superhydrophobic surface with different micro/nano-structures by electrochemical shaping of smooth Cu surface. Appl. Surf. Sci. 353, 1277–1284. https://doi.org/10.1016/j.apsusc.2015.06.162.

Jin, H.Z., Gu, Y., Ou, G.F., 2021. Corrosion risk analysis of tube-and-shell heat exchangers and design of outlet temperature control system. Petrol. Sci. 18 (4), 1219–1229. https://doi.org/10.1016/j.petsci.2021.07.002.

Kan, A.T., Dai, Z.Y., Tomson, M.B., 2020. The state of the art in scale inhibitor squeeze treatment. Petrol. Sci. 17, 1579–1601. https://doi.org/10.1007/s12182-020-00497-z.

Kashchiev, D., Firoozabadi, A., 2002. Nucleation of gas hydrates. J. Cryst. Growth 243 (3–4), 476–489. https://doi.org/10.1016/S0022-0248(02)01576-2.

Khormali, A., Petrakov, D.G., 2016. Laboratory investigation of a new scale inhibitor for preventing calcium carbonate precipitation in oil reservoirs and production equipment. Petrol. Sci. 13 (2), 320–327. https://doi.org/10.1007/s12182-016-0085-6.

Li, H., Yu, S.R., Hu, J.H., et al., 2019. Modifier-free fabrication of durable superhydrophobic electrodeposited Cu-Zn coating on steel substrate with self-cleaning, anti-corrosion and anti-scaling properties. Appl. Surf. Sci. 481, 872–882. https://doi.org/10.1016/j.apsusc.2019.03.123.

Lin, Y.P., Singer, P.C., 2005. Effect of seed material and solution composition on calcite precipitation. Geochem. Cosmochim. Acta 69 (18), 4495–4504. https://doi.org/10.1016/j.gca.2005.06.002.

Liu, D., Hui, F., Ledion, J., et al., 2011. Effectiveness of copper and zinc ions in preventing scaling of drinking water. Environ. Technol. 32 (6), 609–616. https://doi.org/10.1080/09593330.2010.506888.

Liu, Y.C., Zhu, M., Chen, M.Y., et al., 2019. A polydopamine-modified reduced graphene oxide (RGO)/MOFs nanocomposite with fast rejection capacity for organic dye. Chem. Eng. J. 359, 47–57. https://doi.org/10.1016/j.cej.2018.11.105.

Mpelwa, M., Tang, S.F., 2019. State of the art of synthetic threshold scale inhibitors for mineral scaling in the petroleum industry: a review. Petrol. Sci. 16, 830–849. https://doi.org/10.1007/s12182-019-0299-5.

Niu, T., Xu, J., Huang, J., 2014. Growth of aragonite phase calcium carbonate on the surface of a titania-modified filter paper. CrystEngComm 16 (12), 2424–2431. https://doi.org/10.1039/c3ce42322k.

Parsiegla, K.I., Katz, J.L., 2000. Calcite growth inhibition by copper (II): II. Effect of solution composition. J. Cryst. Growth 213 (3), 368–380. https://doi.org/10.1016/S0022-0248(00)00306-7.

Pearson, R.G., 1963. Hard and soft acids and bases. J. Am. Chem. Soc. 85, 3533–3539. https://doi.org/10.1021/ja00905a001.

Plummer, L.N., Busenberg, E., 1982. The solubilities of calcite, aragonite and vaterite in CO_2-H_2O solutions between 0 and 90 °C, and an evaluation of the aqueous model for the system $CaCO_3$-CO_2-H_2O. Geochem. Cosmochim. Acta 46, 1011–1040. https://doi.org/10.1029/93WR02655.

Qian, H.J., Zhu, Y.J., Wang, H.Y., et al., 2017. Preparation and antiscaling performance of superhydrophobic poly(phenylene sulfide)/polytetrafluoroethylene composite coating. Ind. Eng. Chem. Res. 56 (44), 12663–12671. https://doi.org/10.1021/acs.iecr.7b03975.

Ren, G.N., Song, Y.M., Li, X.M., et al., 2018. A superhydrophobic copper mesh as an advanced platform for oil-water separation. Appl. Surf. Sci. 428, 520–525. https://doi.org/10.1016/j.apsusc.2017.09.140.

Sabzi, R., Arefinia, R., 2019. Investigation of zinc as a scale and corrosion inhibitor of carbon steel in artificial seawater. Corrosion Sci. 153, 292–300. https://doi.org/10.1016/j.corsci.2019.03.045.

Sharma, A., Gupta, A.B., 2020. Chemistry of inorganic scaling in full-scale reverse osmosis plants treating brackish groundwater. J. Environ. Chem. Eng. 8 (5), 104108. https://doi.org/10.1016/j.jece.2020.104108.

Tozar, A., Karahan, I.H., 2014. Structural and corrosion protection properties of electrochemically deposited nano-sized Zn-Ni alloy coatings. Appl. Surf. Sci.

318, 15−23. https://doi.org/10.1016/j.apsusc.2013.12.020.

Velayi, E., Norouzbeigi, R., 2019. Fabrication of fluorine-free ZnO/CuO nano-composite superantiwetting surfaces with reversible wettability tuning. Surf. Coat. Technol. 367, 252−261. https://doi.org/10.1016/j.surfcoat.2019.04.007.

Wang, S.S., Meng, H., Li, Y., et al., 2018. Polymer brushes grafted from graphene via bioinspired polydopamine chemistry and activators regenerated by electron transfer atom transfer radical polymerization. J. Polym. Sci., Part A: Polym. Chem. 7, 689−698. https://doi.org/10.1002/pola.29310.

Wang, Y.B., Shang, B., Hu, X.X., et al., 2017. Temperature control of mussel-inspired chemistry toward hierarchical superhydrophobic surfaces for oil/water separation. Adv. Mater. Interfac. 4, 1600727−1600738. https://doi.org/10.1002/admi.201600727.

Wang, Z., Bai, Y., Zhang, H., et al., 2019. Investigation on gelation nucleation kinetics of waxy crude oil emulsions by their thermal behavior. J. Pet. Sci. Eng. 181 (17), 106230. https://doi.org/10.1016/j.petrol.2019.106230.

Xie, A.T., Cui, J.Y., Liu, Y., et al., 2021. Preparation of Janus membrane based on biomimetic polydopamine interface regulation and superhydrophobic atta-pulgite spraying for on-demand oil-water emulsion separation. J. Membr. Sci. 627, 119242−119252. https://doi.org/10.1016/j.memsci.2021.119242.

Yin, Z., Xue, M., Luo, Y., et al., 2020. Excellent static and dynamic anti-icing properties of hierarchical structured ZnO superhydrophobic surface on Cu substrates. Chem. Phys. Lett. 755, 137806. https://doi.org/10.1016/j.cplett.2020.137806.

Zeppenfele, K., 2000. Prevention of CaCO_3 scale formation by trace amounts of copper (II) in comparison to zinc (II). Desalination 252 (1−3), 60−65. https://doi.org/10.1016/j.desal.2009.10.025.

Zhang, C., Li, H.N., Du, Y., et al., 2017. CuSO_4/H_2O_2 triggered polydopamine/poly(-sulfobetaine methacrylate) coatings for antifouling membrane surfaces. Langmuir 33, 1210−1216. https://doi.org/10.1021/acs.langmuir.6b03948.

Zhang, C., Ou, Y., Lei, W.X., et al., 2016. CuSO_4/H_2O_2-induced rapid deposition of polydopamine coatings with high uniformity and enhanced stability. Angew. Chem. 128 (9), 3106−3109. https://doi.org/10.1002/ange.201510724.

Zhang, Z.F., Sun, L., Wu, Z.J., et al., 2020. Facile hydrothermal synthesis of CuO-Cu_2O/GO nanocomposites for the photocatalytic degradation of organic dye and tetracycline pollutants. New J. Chem. 44 (16), 6420−6427. https://doi.org/10.1039/D0NJ00577K.

Zhou, R., Ren, P.F., Yang, H.C., et al., 2014. Fabrication of antifouling membrane surface by poly(sulfobetaine methacrylate)/polydopamine co-deposition. J. Membr. Sci. 466, 18−25. https://doi.org/10.1016/j.memsci.2014.04.032.

Zhu, M.L., Qian, H.J., Yuan, R.X., et al., 2021a. EDTA interfacial chelation Ca^{2+} incorporates superhydrophobic coating for scaling inhibition of CaCO_3 in petroleum industry. Petrol. Sci. 18 (3), 951−961. https://doi.org/10.1007/s12182-021-00558-x.

Zhu, Y.J., Li, H.W., Zhu, M.L., et al., 2021b. Dynamic and active antiscaling via scale inhibitor pre-stored superhydrophobic coating. Chem. Eng. J. 403, 126467. https://doi.org/10.1016/j.cej.2020.126467.